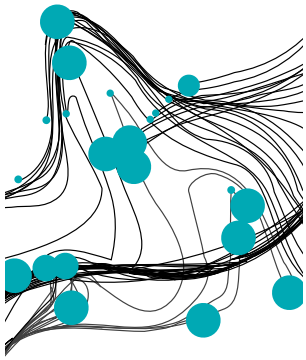

RAM ROBOTICS AND MECHATRONICS

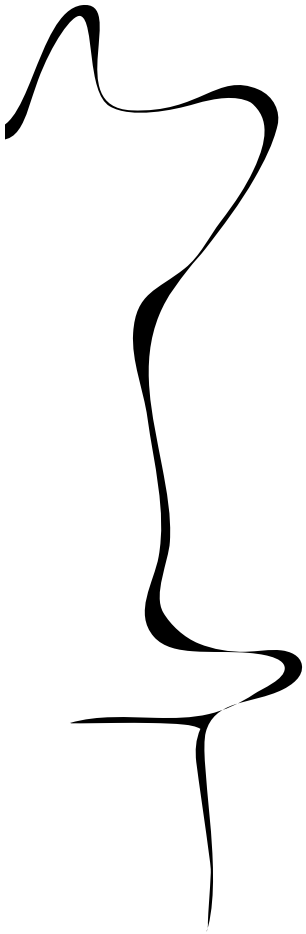

OXYFORCE: DEVELOPMENT OF A NEAR INFRARED SPECTROMETRY SENSOR TO DETECT HYPOXIA FOR BREAST CANCER RESEARCH AND DIAGNOSTICS

M. (Marloes) Pijpker

BSC ASSIGNMENT

Committee:
dr. ir. K. Niu
B. Lan, MSc
dr. I. Tamadon

December, 2024

081RaM2024
Robotics and Mechatronics
EEMCS
University of Twente
P.O. Box 217
7500 AE Enschede
The Netherlands

UNIVERSITY OF TWENTE. | TECHMED CENTRE
UNIVERSITY OF TWENTE. | DIGITAL SOCIETY INSTITUTE

Abstract

Breast cancer takes a large toll on society, and early prevention and detection reduces costs and improves prognosis for patients. In tumors, metabolic rate is higher, together with oxygen consumption. This can cause regions of lower oxygen saturation. In Near InfraRed Spectroscopy, the absorbance of light is used to compute concentrations of substances. In the body, oxygen binds to heme in red blood cells. If oxygen is bound to heme the red blood cells change color. If a lower ratio of bounded to non bounded heme can be measured, it could be possible for a lower oxygen saturation to be detected by a Near Infrared Spectroscopy (NIRS) sensor. The NIRS sensor developed in this report shows promising results in being able to measure a difference in oxygen saturation over time. The sensor did show some inconsistencies in drift and mean output, what could indicate incorrect calibration or measurement methods.

Contents

Chapter 1

Introduction

1.1 Breast cancer

Breast cancer comprises 11.7% of all new cases of cancer and 6.9% of all new deaths of cancer globally in 2020. It is a type of cancer with one of the highest prevalences, and of the highest cancer mortalities[1]. As found by Vondeling et al; 'Annually, breast cancer in the Netherlands is responsible for approximately 3100 deaths, 26,000 life years lost, 65,000 Disability Adjusted Life Years (DALYs) and an economic burden of 1.27 billion EUR.' These numbers are found when averaging between 1990 and 2014. This economic burden is found in care, prevention, drugs and lost productivity [2]. If breast cancer is diagnosed in its early stages the patients' survival rate significantly improves [3]. These statistics reveal the impact early diagnosis can bring. Non-invasive and inexpensive diagnostic tools can provide a base for wide screening methods. In this way, total healthcare costs could be lowered and both life years lost and disability adjusted life years could be lowered.

1.2 Vascular system

One of the main functions of blood is to transport oxygen from the lungs to all cells in the body, so the cells can perform their specialized functions. The blood moves through the body via the vascular system, and the heart pumps to move the blood through this system. The vascular system contains two circuits originating from the heart, see figure 1.1. The pulmonary circuit provides a path to the lungs, where blood is loaded with oxygen. The systemic circuit provides a path to the cells, where blood transfers its oxygen to the tissues.
The systemic circuit is often divided into three types of vessels, dependent on direction and function: arteries, capillaries and veins. Arteries transport blood from the heart to the tissues, and veins transport the blood from the tissues to the heart. The capillaries provide the site for the transfer of oxygen from blood to tissue. The vessel walls of the capillaries are designed for gas exchange as

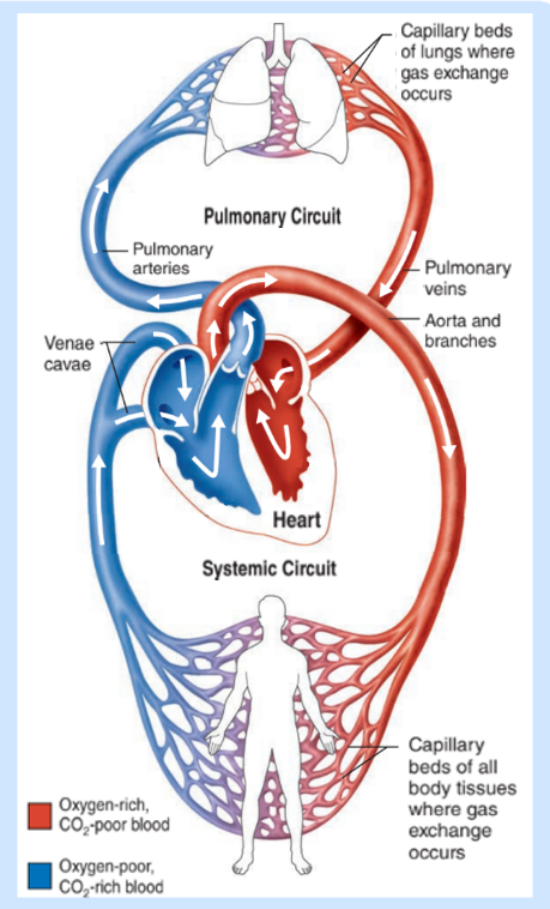

Figure 1.1: The simplified, schematic human vascular system. Oxygen rich blood is pumped by the heart throughout the body, where in the capillaries oxygen it is transferred from the blood to the tissues. The then oxygen-poor blood returns to the heart and later to the lungs, where it is re-oxygenated in the capillaries of the lungs. After this, the again oxygen rich blood returns to the heart to restart the cycle. [4]

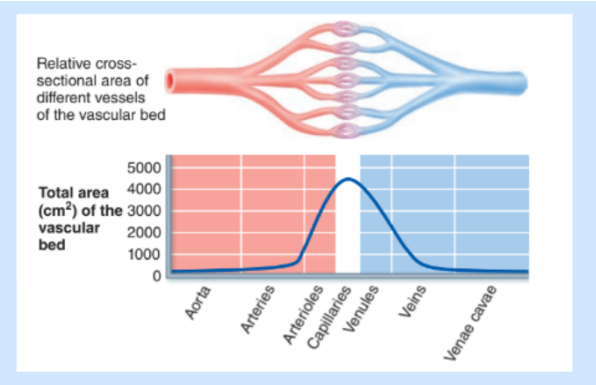

Figure 1.2: Total area of the vascular bed, plotted for the type of blood vessel. Capillaries have a much higher surface area than other types of blood vessels[4].

they are much thinner than venal or arterial blood vessel walls. Their total area is also many times larger, as seen in figure 1.2. A combination of these qualities mean that most gas exchange occurs at the capillaries.
The flow of blood through the vessels is propelled by the heart. As the muscles of the heart contract, the fluid pressure in the heart temporarily increases greatly, and blood flows out through the arteries while heart valves make sure the blood does not flow back. The fluctuating high pressure created by the contraction of the heart is known as the pulse. This pulse is mostly felt in the arteries, as seen in figure 1.3 and can even be felt when you put your finger to your jugular artery for example [4].

1.3 Blood oxygen and color

In blood, oxygen is mostly transported by red blood cells. Red blood cells are doughnut-shaped cells of about $7.5\mu m$ in diameter[4]. Oxygen easily binds to iron in its polypeptide-chains of globin. Globin is present in pairs of four in hemoglobin molecules, that are present in large numbers in red blood cells. The hemoglobin molecule is as seen in figure 1.4. When an oxygen molecule binds to the iron atom in the heme, the polypeptide molecule slightly changes its shape. This change in shape causes a slightly different interaction with light. As a result, hemoglobin that has oxygen bound to it has a different color than hemoglobin that has not [6, 7]. Oxygen-loaded hemoglobin is called oxyhemoglobin (HbO2), and is ruby-red of color. Oxygen-lacking hemoglobin is called deoxyhemoglobin (Hb) and is darker red of color, see figure 1.5B. The absorption spectrum expressed in the molar extinction coefficients is as seen in figure 1.5A. It is seen that for the 660 nm, which is red, the extinction coefficient is much larger for Hb than HbO2, what sets up this difference in color.
Oxygen saturation describes the ratio between Hb and HbO2 and is defined

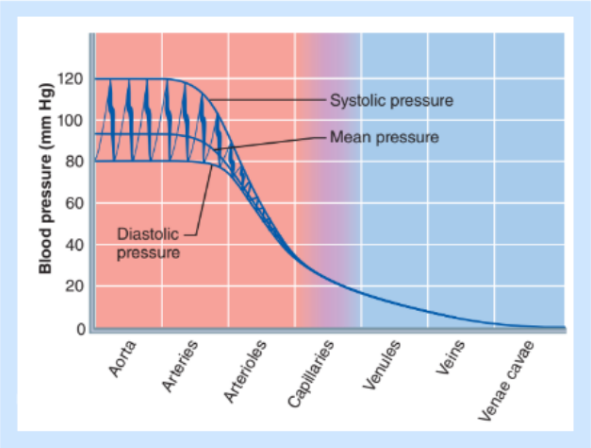

Figure 1.3: Blood pressure per vessel type of the systematic circuit. It is visible that the blood pressure is highest in the aorta, and lowest in the venae cavae. The pulse caused by contraction of the heart is more present before blood enters the capillaries, and much less present with regards to the arterial vessel when entering the capillaries and venal vessels[4].

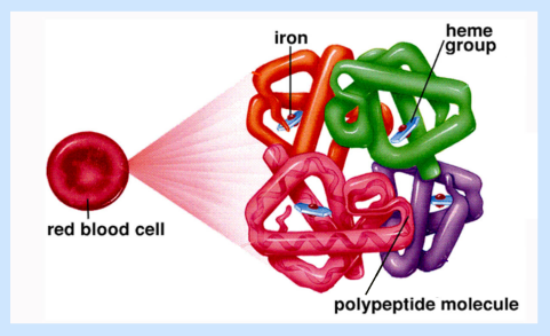

Figure 1.4: A schematic representation of red blood cells (left) and hemoglobin(right) [5].

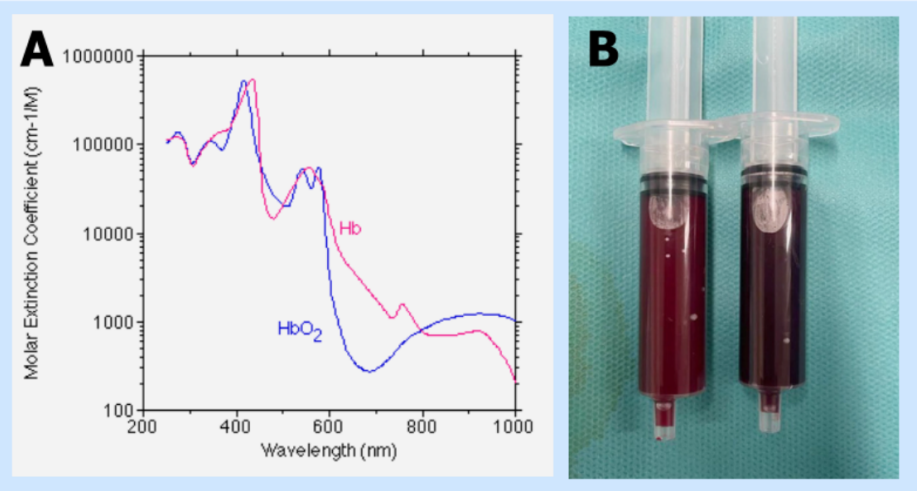

Figure 1.5: A)Extinction coefficients of oxy- and deoxyhemoglobin. There are differences between the levels in which they absorb light. Where the spectra in the range under 600 nm are more similar, there are big differences in the range of 600 nm to 1000 nm. B) Two syringes with blood, showing the visual difference in color. Arterial blood (left) contains more bound oxygen, and is lighter of color. Venal blood (right) contains less bound oxygen and is darker. [8, 9].

as the percentage of hemoglobin molecules in blood that are bound to oxygen molecules in contrast to all hemoglobin. Normal venous oxygen saturation in rest as measured in the pulmonary arteries (see figure 1.1) is around 70% to 75% saturated. Normal arterial oxygen saturation in the systemic circuit in rest lies between 95% and 99% [10]. This is important to consider, as the oxygen saturation in blood or its deviation from the norm can give information about the health of a patient.

About 98% of all oxygen in vessels is bounded to hemoglobin, and 2% is dissolved in blood plasma[6]. This is relevant in the blood vessels. Oxygen travels from high to lower pressure areas. Especially in the capillaries with high surface area and thin walls this dissociated oxygen travels through the vessel walls and into the tissues. Hemoglobin normally will stay in the vessels[11]. This means that from the existing vessels, an oxygen gradient is formed in tissue with a higher partial pressure at the arterial end of a capillary and a lower partial pressure at the venous end of a capillary. If the pressure difference over distance is higher, there is a higher flux of oxygen. So also, if the demand of a cell is higher, the flux of oxygen to the cell will be higher[6].

1.4 Oxygen consumption and supply in tumors

Hypoxia, or oxygen deprivation in tissue, is a key characteristic of breast cancer. A tumor needs a great amount of nutrients and oxygen, which it receives from the surrounding capillaries [12]. As the demand is higher, the higher difference in pressure over distance can create a larger oxygen flux. However, existing vascularisation is often not sufficient to deliver enough oxygen, as the tumor grows and distance to the existing blood vessels is too large for some cells. A response can form that promotes formation of new blood vessels by producing hypoxia-induced-factors[13]. However, vascularisation as a result of these new blood vessel in tumors have structural and functional deformities. This adds to inadequate delivery of oxygen to the tumor tissue [14]. This greater demand and lower supply of oxygen both add to the strength of a hypoxic environment. Hypoxia is however not present in every tumor. Measuring the hypoxia induced factors can give an indication for prevalence. Using this, 25% to 40% of invasive breast cancers can be categorized as hypoxic [15].

1.5 Measurement and imaging of hypoxia

A lower local oxygen saturation in capillaries and veins can point to a higher oxygen consumption. This can in turn point to a higher local metabolic rate which can signal to a tumor being present [16]. If reliably measuring hypoxia in human tissue is possible, this could be used for cancer detecting and monitoring. In the next part, some blood/tissue oxygen saturation sensing methods will be introduced and compared.

1.5.1 Blood Gas Analysis

Blood gas analysis is considered the golden standard when measuring oxygen saturation in blood. Blood is taken with a syringe from anywhere in the vascular system, and is tested for the partial pressure of oxygen which is directly related to oxygen saturation via the oxygen saturation curve[4]. Arterial and venal blood oxygen as determined by the blood gas analysis are called SaO_2 and SvO_2, respectively[17, 6].

1.5.2 MRI and PET

With MRI (Magnetic Resonance Imaging) and PET (Positron Emission Tomography) indications of hypoxic tissues can be imaged. The PET modality makes use of radioactive tracers. Certain tracers will pool in hypoxic cells and by imaging the sources of gamma rays hypoxic regions can be detected. A disadvantage of PET is the need of the injection of this tracer. A PET scan also takes more than an hour, so it is not feasible to use this for exploratory screening [18, 19]. MRI is based on excitation and relaxation of hydrogen atoms using radiofrequency waves and strong magnets. Hb and HbO2 have different

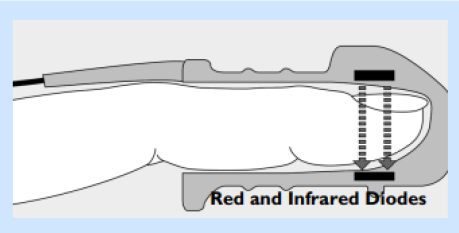

Figure 1.6: Typical setup of a transmissive pulse oximetry sensor. A finger is placed in the pulse oximeter, where light is emitted on one side by a light source and received on the other side by photodiodes. Earlobes are also often used for transmissive pulse oximetry[20].

magnetic properties, and a scan can indicate hypoxia. MRI is non invasive. [19]. It is however very expensive and a scan takes a long time, so it is not feasible to use this for exploratory screening.

1.5.3 Pulse oximetry

With pulse oximetry the SaO_2 can be approached. It is very non-invasive, inexpensive and has really accurate readings. It uses a combination of the Lambert-Beer law, the differing extinction coefficients of Hb and HbO2 for some wavelengths and the pulse. A typical setup is as seen in figure 1.6. Light emitters of two or more peak wavelengths in the red to infrared spectrum are placed on one side, and light detectors of the same wavelengths are placed on the other side. Pictured is a transmissive mode. Reflective mode is also often used. Here the sensors and light sources are placed on the same side of the tissue at some small distance from each other. When using the reflecting mode, you can also measure on areas that are too thick for transmissive mode. This is possible because of the scattering properties of light in tissue; reflective and transmissive mode are computationally the same for pulse oximetry wavelengths, as long as the absolute pathlength is at least 1mm[21].

When light travels through a tissue, there will be less light that exits the tissue than it enters. Part of it is absorbed and part of it is scattered, and the intensity of light decreases the further it travels as pictured in figure 1.7. The amount of light that is absorbed over distance is different for each wavelength through each tissue. The Lambert Beer equation shows this relation in a solution with an absorber with a concentration C. It links the transmitted light to the incident light through a solution at a certain wavelength, and shows it is dependent on its pathlength, concentration and the molar extinction coefficients of the solution it travels through. It is described for a uniform solution as[7]:

$$I(\lambda) = I_0(\lambda)e^{-\mu(\lambda)dC} \tag{1.1}$$

Here is $I(\lambda)$ the intensity at a point for a wavelength, $I_0(\lambda)$ the intensity of

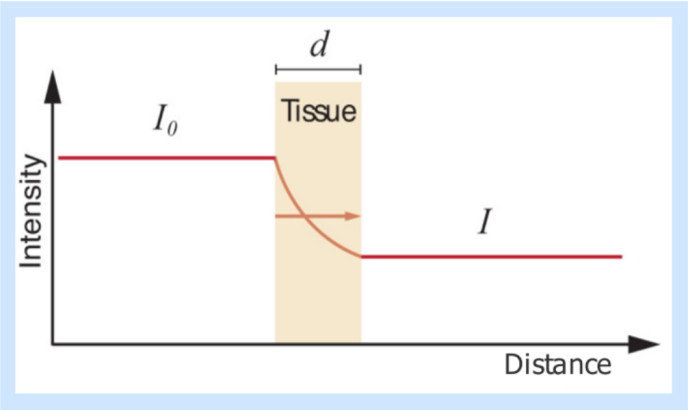

Figure 1.7: The extinction of light through a tissue. Here is I_0 the intensity of light that enters the tissue, and I the intensity of light that leaves the tissue[7].

the incident light at that wavelength, $\mu(\lambda)$ the extinction coefficient for that material for that wavelength, and d the pathlength of the light through the material. C shows the concentration of the chromophore that is connected to the extinction coefficient. Because you can link the amount of light that goes through a substance to the concentration of a chromophore, the Lambert-Beer equation forms the basis for pulse oximetry. From this equation, you can also see that the smaller the extinction coefficient, the higher the intensity is of the transmitted light if all else stays the same. As seen in figure 1.5, light with a wavelength larger than 600 nm is able to penetrate deeper relative to other wavelengths. That is why light in the red to infrared spectrum is often chosen for lambda; less light is absorbed in the tissue, increasing the amount of signal.

While the heart contracts, the pressure in the artery goes up and the blood vessel expands. This is causing the fraction of blood and tissue to change. Because there is more of the chromophores Hb and HbO2 in the system, you can see this in the amount of light absorbed[21, 4]. See also figure 1.8. Because this action repeats itself an pulsatile element is visible. By isolating only the pulsatile element of the measurement, most absorption caused by elements that are not blood like tissue and bone is subtracted. At that point, signal that is left will be from the pulsatile blood. Using the extinctions coefficients of oxy- and deoxyhemoglobin as seen in the spectrum in figure 1.5, it is possible to compute the ratio of each chromophore; Hb, and HbO2. From ratio the oxygen saturation in the blood can be determined. This resultant oxygen saturation in the pulse is called SpO_2[22].

SpO_2 values usually differ some, but not a lot from the invasively determined SaO_2 values[21]. The SpO_2 value is often used to non-invasively approach the SaO_2 value, as the difference between these values are often less than 2%[23].

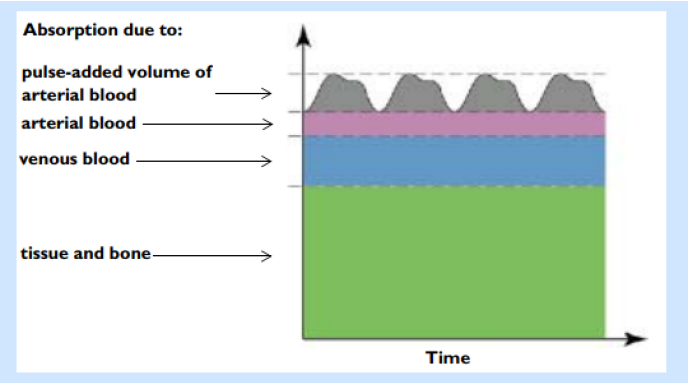

Figure 1.8: Absorption of light in tissue. Percentual contributions of each of the elements is not proportional to reality, but serves as an example[20].

1.5.4 Near InfraRed Spectroscopy

Near InfraRed Spectroscopy (NIRS) is a method related to pulse oximetry, and some of the same basic principles as for pulse oximetry are used with some key differences. It also uses light and the Lambert-Beer equation to determine the concentration of Hb and HbO2 non-invasively. The first key difference lies in the target substance; with NIRS, the oxygen saturation of blood in the combined blood vessels and tissue can be approximated. The pulsatile elements of the red and infrared data are not isolated, so the absorption that is caused by other tissues and non-pulsatile blood is also taken into account. Background components of the measurements are not filtered out including muscle, bone and fat. Also, venous and capillary blood is not filtered out.

Because this is not filtered out, is it possible to measure the contributions from venous and capillary blood. However, this also means that contributions from other tissues will influence signal. From the recieved signal, using the earlier given Lambert-Beer equation and the extinction coefficients of oxy- and deoxyhemoglobin the oxygen saturation in the blood can be approximated. The computations will be found in section 2.5.

Two of the non-blood contributions are deoxymyoglobin (Mb) and oxymyoglobin (MbO2). These are present in the muscle, and are oxygen carriers in the myocyte. It is not yet clear how much of the NIRS signal originates from either; estimations range from 10% to 90%. However, their extinction coefficients are very similar to those of Hb and HbO2, respectively. Relevant peaks in the absorption spectrum originate from the same heme group, and thus are both dependent on whether oxygen is bound to it. Because of these reasons they are often referred to as a sum in the context of NIRS; oxy[heme] and deoxy[heme]. This is most important to take into account when measuring muscular areas.

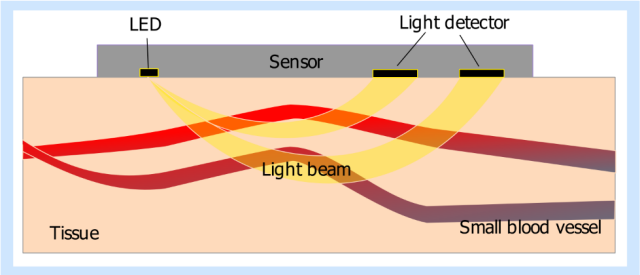

Figure 1.9: Schematic representation of light beams in tissue. It is possible to collect data from multiple depths by varying the distance between light source and light detector.

Muscle changes shape upon contraction, which is why contraction will give large artefacts[24, 7].

NIRS is now used for functional neuroimaging. It does not measure absolute values of oxygen saturation because of the influence of other tissue. Instead it measures oxygen saturation relative to other areas of the brain or relative to itself at an earlier point in time. In this way areas with higher oxygen consumption may be identified. Values determined by NIRS are defined as the tissue oxygen saturation, or StO_2.

Using NIRS, multiple penetration depths can be achieved. Due to scattering, light diffuses through the tissue. When looking at the bulk light that a certain light detector has received from a certain light source, it is found that the majority of light has taken a 'banana'-shaped path as seen in figure 1.9. This means that on average, the received signal will give information from that depth[25, 26].

The influence of scattering on transmitted intensity and specifically pathlength is an important factor. Red and infrared light are very strongly scattered in tissue, which means that light has experienced multiple scattering events in the tissue before reaching the detector. This makes the pathlength of light a lot longer, and means that the absolute distance between the detector and light source is not reflective of pathlength. Instead of only pathlength, the differential pathlength factor (DPF) is often used as a scalar to absolute pathlength. This DPF is dependent on multiple factors. E. G., not every photon follows the same path and different tissues have different scales of homogeneity and density. Temperature also changes the value of the DPF over time[7]. Incorporation of this is in the Lambert Beer equation as seen in equation 1.1 gives:

$$I(\lambda) = I_0(\lambda)e^{-\mu(\lambda)\cdot d\cdot C\cdot DPF} \tag{1.2}$$

By not isolating the pulsatile part, the relevant fraction of venous to arterial blood could be different than for pulse oximetry. As SaO_2 is relatively stable, a change in SvO_2 and muscle oxygen saturation could be better visible with NIRS than pulse oximetry.

1.6 Research goal

As said in section 1.4, a local lower oxygen saturation in capillaries and veins can point to a higher demand of oxygen in tissue. This can in turn point to a higher local metabolic rate, which can point to a tumor. While there are more reasons for a lower local oxygen saturation, this property could be used to non-invasively and inexpensively direct possible patients to seek early diagnosis and care. This can possibly improve quality of life for patients and decrease pressure on healthcare.
In this report the possibility of using NIRS as a method for exploratory tumor detection is presented. It is part of developmental research for OxyForce, a diagnostic tool that uses detection of tissue stiffness and oxygen saturation to screen a breast for tumors. Some of this work is based on earlier work done for the same project. This report is exploratory, so the question is whether the developed code in combination with the light sensors is able to differentiate in vivo differences between high and low oxygen saturation. Together with this the used calibration method will also be explored.

Chapter 2

Methods and Materials

2.1 Hardware

Most of the setup for the hardware is based on the setup made for a pulse oximetry sensor made by Ellen Juffermans. This setup uses a Arduino Uno R3 micro-controller and 2 GY MAX30102 pulse oximeter sensors. A PCA9548A I2C multiplexer is used to direct multiple sensors at once. The setup is shown as in figure 2.1. A close-up of the sensor is as seen in figure 2.4. The LEDs on the Gy-MAX 30102 sensor emit light with peak wavelengths at 660 nm or 880 nm. The photodiodes read the intensity of light for these same wavelengths. The LED and photodiode are present on the same side of the tissue, this means that reflective mode NIRS wil be used. For clarity; the sensor is defined as the MAX-30102 unit, the LED is the light emitter on the sensor, and the photodiode is the light detecting unit on the sensor.

2.2 Software: acquiring the data

In total, three pieces of software are used to drive the sensors, interact with the setup and process the data. The first is ran and uploaded in Arduino IDE, and the other two are ran in Microsoft VS code.

2.2.1 Driving the sensors

The software that drives the sensors is written in C++ and is uploaded to the micro-controller. It activates the LEDs, and lets the photodiode read off the produced photocurrent, which is the output that the computer receives. It sets a frame rate of 50 reading per second with an averaging of 2 frames per output value. It has an ADC range of 0.16384 mA. It is adjusted to have 2 sensors, however this can be modified. This software is modified from that received by Ellen Juffermans.

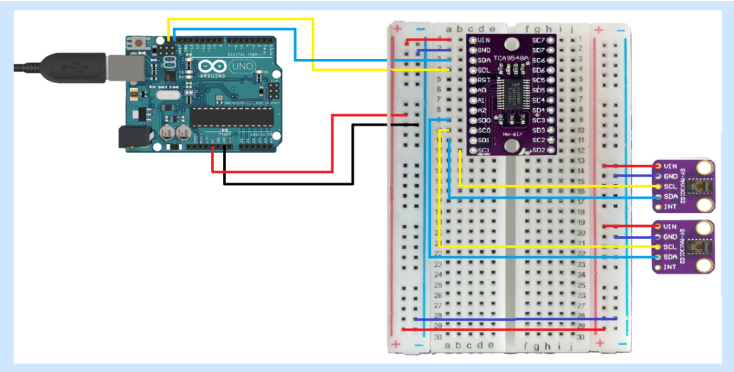

Figure 2.1: Circuit drawing of the setup of the NIRS sensor. The sensors are connected to a breadboard, which is connected to the Arduino micro-controller. In the middle of the breadboard a multiplexer manages the in and output of multiple sensors. Here, 2 light sensors are used, but up to 8 sensors can be linked as needed

2.2.2 Interacting with the sensors

The software that interacts with the sensors is written in python. It interprets the data as received via the microcontroller. While running, an interface pops up where you can choose to start and stop measuring, and to start and stop recording the measurement. This recording is then saved to a file that is saved to your computer. This software is mostly received from Ellen Juffermans, but modified to fit the NIRS method. The output is a text file that contains a list of photocurrent data for each wavelength and sensor. This data will be further processed, plotted and compared in the piece of software, as seen in section 2.5.

2.3 Calibration: determining incident light

To be able to determine the concentration of a substance, it is necessary to know the incident light as referenced to in equation 1.2. This will be determined as explained in the following section.

2.3.1 Setup

During calibration, the sensor is placed directly on a mirror. Both pieces of software as described in section 2.2 will be ran, and the amount of photocurrent that is detected by the photodiode will be recorded for a chosen amount of time. This resultant photocurrent will be a combination of the produced light by the LED, and any lingering background light. To minimize background light, the calibration measurement is done in the dark. The setup is as seen in figure 2.2. This calibration measurement will last at least 20 seconds. The goal is to record the amount of detected photocurrent when there is no absorption or scattering.

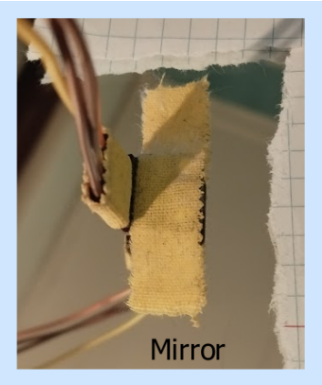

Figure 2.2: Picture of the setup of a calibration measurement. Paper around the edges is added for clarity, and is not present in actual calibration. The tape keeps the sensor in place. Note that all measurements are done in the dark

In total, three calibration measurements will be done. Two of these are linked to a set, and will be done on the same day and will represent as the incident light for these sets. The third measurement is done separately, to be able to compare more data.

2.3.2 Computation

However, not all the light that is emitted by the LED is measured by the photodiode. There is a three mililimeter thick glass layer over the mirror, which increases the distance between the light source and photodiode. The LED does not emit light in a parallel fashion, LEDs are often approximated as Lambertian emitters [27, 28], as pictured in figure 2.3. This means that the intensity of emitted light is dependent on the angle to the normal axis of the source.

The situation as visible in figure 2.2 is schematically displayed in figure 2.5A

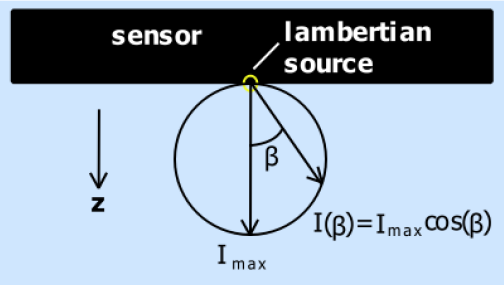

Figure 2.3: Representation of the intensity pattern of light of a Lambertian source. The intensity is dependent on the angle to the normal axis of the sensor.

and B. The visible symbols are as defined in table 2.1. If the LED emits light in a Lambertian pattern, then a lot of light will not reach the detector. The photocurrent that is detected by the photodiode is not representative the total output of the LED. A closeup of the optical unit of the sensor is seen in figure 2.4.

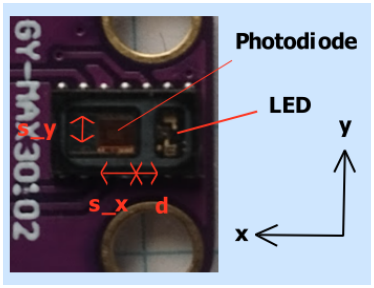

Figure 2.4: Close-up of the optical unit of the sensor. Some dimensions and symbols are defined.

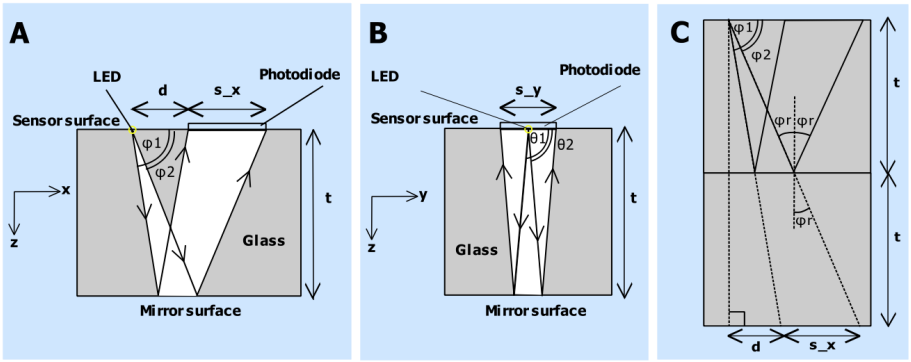

Figure 2.5: Schematic representation of the light in the calibration setup. Some dimensions and symbols are defined. Here the light that is marked in white reaches the detector, and the light that is grey does not. Two lightrays with angles are drawn. Angle 1 shows the maximal angle with respect to the sensor surface that reaches the photodiode in both figures, and angle 2 shows the minimal angle with respect to the sensor surface that reaches the phototdiode in both figures. The planes that are defined are in accordance with the planes as defined in figure 2.4. A) Schematic view in the x-z plane. B) Schematic view in the y-z plane. C) Supporting graphic for computation of the angles. Derived from A.

The escaping light makes it so incident photocurrent is not equal to the photocurrent as detected during the calibration. To approximate the incident photocurrent, some computations are done. For this the following assumptions and/or simplifications are made:

Symbol	Value	Unit	Meaning
d	1	mm	Distance between the LED and photodiode
s_x	1.4	mm	Size of photodiode in the x direction
s_y	1	mm	Size of the photodiode in the y direction
t	3	mm	Thickness of the glass
ϕ		rad	Angle of light with respect to the x-axis
θ		rad	Angle of light with respect to the y-axis
β		rad	Angle of light with respect to the z-axis
N		#	Photocurrent count
N_0		#	Incident photocurrent count
N_A		#	Photocurrent count on the sensor
N_{max}		#	Photocurrent in the direction normal to the sensor

Table 2.1: Clarification of some symbols.

- There is perfect contact between the glass and sensor;
- The glass does not scatter or absorb light;
- The sensor surface reflects no light;

First the angles as seen in 2.5A and B will be computed. Using the supporting graphic C, it is seen that the angle to their respective axes are equal to:

$$\phi_1 = 0.5\pi - arctan\left(\frac{d}{2t}\right) = 0.5\pi - arctan\left(\frac{1}{6}\right) = 1.4056 \tag{2.1}$$

$$\phi_2 = 0.5\pi - arctan\left(\frac{d+s_x}{2t}\right) = 0.5\pi - arctan\left(\frac{1+1.4}{6}\right) = 1.1903 \tag{2.2}$$

$$\theta_1 = 0.5\pi - arctan\left(\frac{-0.5s_y}{2t}\right) = 0.5\pi - arctan\left(\frac{-0.5}{6}\right) = 1.4876 \tag{2.3}$$

$$\theta_2 = 0.5\pi - arctan\left(\frac{0.5s_y}{2t}\right) = 0.5\pi - arctan\left(\frac{0.5}{6}\right) = 1.6534 \tag{2.4}$$

A Lambertian source is described with[29]:

$$I(\beta) = I_{max} \cdot cos(\beta) \tag{2.5}$$

Where I_{max}, also seen in figure 2.3, lies parallel to the z-axis in the defined coordinate system. The angle β is dependent on θ and ϕ in the following relation:

$$\rho sin(\theta)sin(\phi) = z = \rho cos(\beta) \tag{2.6}$$

Besides that, the count that is determined by the photodiode is proportional to the surface of the photodiode, and to the intensity of the light that hits the photodiode; $N \propto A \propto I$ [30]. This means that also:

$$N(\beta) = N_{max} \cdot cos(\beta) \tag{2.7}$$

This is for the photocurrent with an angle β to the z-axis. For the photocurrent on a surface, you need to integrate over that surface. Integrating over that surface, while substituting equation 2.6 into equation 2.7 considering $\rho = N_{max}$ gives:

$$N(\phi, \theta) = \iint_A N_{max} \cdot sin(\theta) sin(\phi) dA \tag{2.8}$$

To find the incident photocurrent, the surface A will be the semi-sphere. This means that $0 \leq \phi \leq \pi$ and $0 \leq \theta \leq \pi$:

$$\begin{aligned} N_0 &= \int_0^{\pi} \int_0^{\pi} N_{max} \cdot sin(\theta) sin(\phi) d\phi d\theta \\ &= \int_0^{\pi} N_{max} sin(\theta)(-cos(\pi) + cos(0)) d\theta \\ &= N_{max}(-cos(\pi) + cos(0))(-cos(\pi) + cos(0)) \\ &= N_{max}(1+1)(1+1) = 4N_{max} \end{aligned} \tag{2.9}$$

From the calibration measurement, we measure a count N_A over the photodiode area A. This is over the known angles. This means that $\phi_2 \leq \phi \leq \phi_1$ and $\theta_2 \leq \theta \leq \theta_1$. Filling this in into equation 2.8 gives:

$$\begin{aligned} N_A &= \int_{\theta_2}^{\theta_1} \int_{\phi_2}^{\phi_1} N_{max} \cdot sin(\theta) sin(\phi) d\phi d\theta \\ &= N_{max} \int_{\theta_2}^{\theta_1} sin(\theta)(-cos(\phi_1) + cos(\phi_2)) d\theta \\ &= N_{max}(-cos(\theta_1) + cos(\theta_2))(-cos(\phi_1) + cos(\phi_2)) \\ N_{max} &= \frac{N_A}{(-cos(\theta_1) + cos(\theta_2))(-cos(\phi 1) + cos(\phi 2)} \end{aligned} \tag{2.10}$$

Combining equation 2.9 and 2.10 gives:

$$\frac{N_0}{4} = \frac{N_A}{(-cos(\theta_1) + cos(\theta_2))(-cos(\phi_1) + cos(\phi_2))} \tag{2.11}$$

The incident photocurrent is found as a function of the detected photocurrent and known photodiode. Finally, substituting equations 2.1-4 into equation 2.11 gives:

$$N_0 = \frac{4N_A}{(-cos(\theta_1) + cos(\theta_2))(-cos(\phi_1) + cos(\phi_2))} \tag{2.12}$$

$$\begin{aligned} &= \frac{4N_A}{(-cos(1.4876) + cos(1.6534))(-cos(1.4056) + cos(1.1903))} \\ &= \frac{4N_A}{0.03426} = 117 \cdot N_A \end{aligned} \tag{2.13}$$

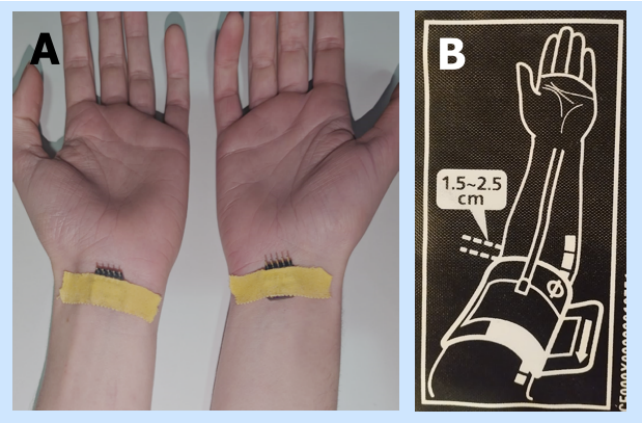

Figure 2.6: Images of the sample setups. A) Picture of sensor placement. Wires that connect the sensors to the board are disconnected for clarity. Yellow tape hold the sensors in place during the samples. B) Instruction of placement of the blood pressure cone cuff.

This means that the total emitted photocurrent by the LED approximately 117 times bigger than the photocurrent detected by the photodiode in this sensor configuration.

2.4 Measurements: inducing changes in blood oxygen saturation

To prove the sensor is able to measure oxygen saturation differences in magnitudes present in the human body, blood flow occlusion is used to temporarily and locally lower oxygen saturation. A commercially available blood pressure measurement cuff is used.

2.4.1 Setup and overview

When determining if the sensors can measure a change in oxygen saturation, they will be tested on the wrists. One sensor will be attached to each wrist, and a blood pressure cuff is placed on one arm as per its instructions. In this way, a difference in oxygen saturation will be induced by the blood pressure cuff in one arm. An image of this is seen in figure 2.6. Note that again, all measurements are done in the dark.
The subject is placed in a sitting position with the arms laid in a relaxed position. In this way the sensors and its wires have minimal contact with external objects that could influence readings, while the subject is able to rest and not tense their muscles. In this way movement and muscle activation is minimized. A second person navigates the software, starts the recording, activates inflation

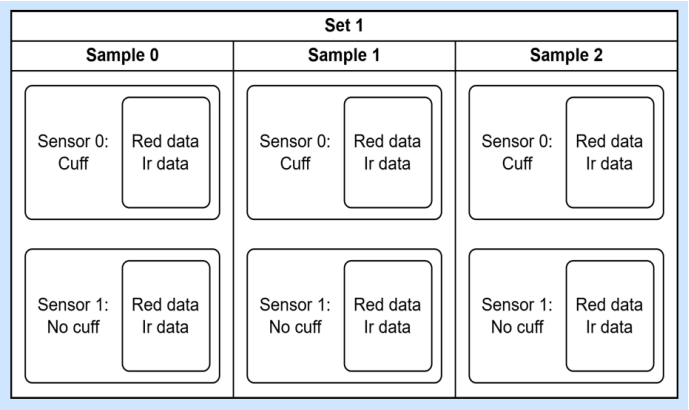

Figure 2.7: Overview of measurement set 1. Every set contains 3 indentical samples, and every samples contains 2 sensors. Every sensor then produces 2 datastrings. In total, there will be two sets where set 2 is a repetition of set 1.

of the cuff and ends the measurement. More information on timing in the measuring cycle is found in figure 2.8. The subject waits for at least 5 minutes in the measuring position before starting a new sample, to let the StO_2 return to baseline. It is attempted to minimally adjust the sensors in-between samples.
In total, two identical, separate sets of measurements are done. See figure 2.7 for an overview of set 1. Each set of measurement contains identical samples 0, 1 and 2, which each in its turn contains sensors 0 and 1. Sensor 0 will be attached to the arm with the cuff, sensor 1 will be attached to the arm without the cuff. Each sensor emits and detects light of two wavelengths, 660 nm (red) and 880 nm (infrared). While the sets are done over multiple days, each of sensors used and named are physically also the same sensors, to investigate stability of a sensor over differing days.

2.4.2 Measuring cycle

To prove the sensor is able to measure oxygen saturation differences of magnitudes present in the human body, blood flow occlusion is used to temporarily and locally lower oxygen saturation. The pressure the blood pressure cuff produces over time in the measurements is as seen in figure 2.8. The diastolic and systolic pressure as seen in the figure are individual to the subject.
A typical resultant tissue oxygen saturation curve is as seen in figure 2.9. First there is a baseline, which is before the cuff is activated. The StO_2 is expected to be stable. Then there is decrease in StO_2 as the cuff is inflated and blood flow occlusion takes place as the pressure rises above the systolic and diastolic blood pressure. As soon as the cuff is released, the StO_2 value is expected to approach the baseline value again, which it overshoots before returning to baseline[31, 32].

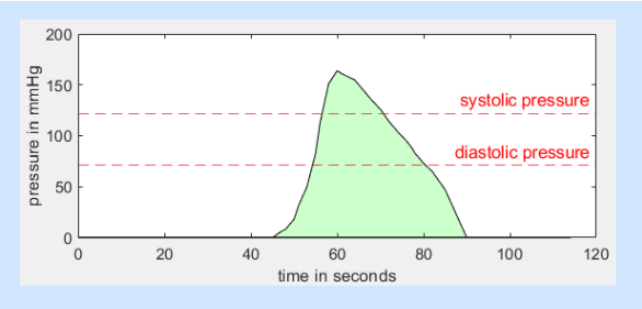

Figure 2.8: The pressure of the pressure cuff during the measuring cycle. First, there are 45 seconds of no pressure before the cuff is activated. Here the baseline StO_2 can be determined. After that, the cuff is activated and the pressure is build up to around 150 mmHg, which is above the systolic and diastolic pressure. After that, the pressure is gradually released and blood flow will be restored.

Because the deflation of the commercial cuff used in this report does not

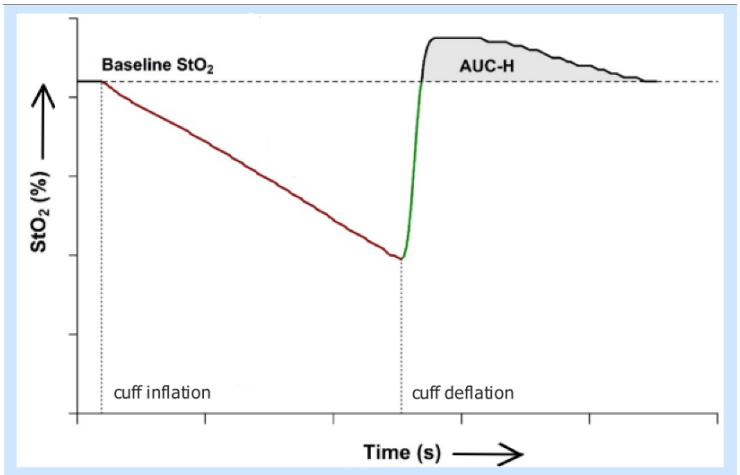

Figure 2.9: A typical tissue saturation curve when tissue is subject to a vascular occlusion. Visible is a baseline before occlusion, a slow decrease in StO_2 during occlusion, and a fast increase with overshoot after release of the occlusion[31]. Note that in the test above a cuff was used of uniform pressure, and for the measurement in this report a varying pressure is used.

immediatlely let the pressure of the cuff drop under the systolic pressure, it is expected that the visible peak in measured StO_2 does not coincide in time with the peak pressure at 60 seconds. The overshoot after deflation can be explained by the reaction fo the body to oxygen deprivation. While the cuff is inflated, the body notices the oxygen depraved tissue. The body temporarily releases

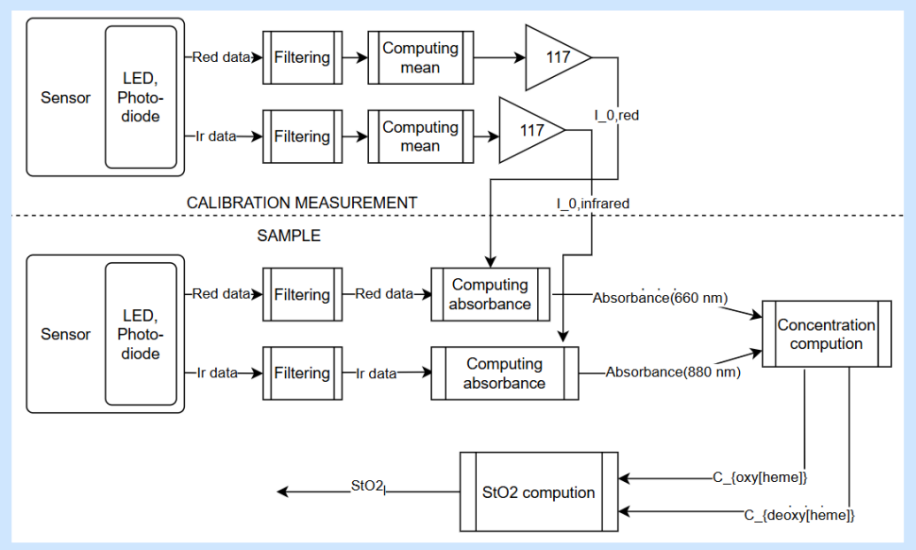

Figure 2.10: Flowchart of the computation from the detected data to StO_2 values. To be able to compute the StO_2, you need both wavelengths on the sensor, and a separate calibration measurement. Notice that this is for one sensor in the sample, and that there are two sensors in a single sample. The flowchart is the same for sensor 0 and 1.

artery dilating compounds. When the cuff is released, the widened arterioles temporarily allow a large influx of oxygen-rich blood[33].

2.5 Software: Processing the saved data

The software that processes the data is written in python. It reads and formats the data produced by the previous software, as seen in section 2.2.2. The input is thus this same list of photocurrent data, which is unpacked and processed by the functions. The processing of the data is summarized as in figure 2.10. Each component of the flowchart will be discussed in the next sections.

2.5.1 Drift removal, filters and interpolation

First the data is loaded from the saved file and put in a library, to order all the data according to figure 2.7. Missing values are interpolated. If the lines were deleted instead of interpolated, the timeframe will be shifted, and not represent reality. If any indices are missing, they are replaced with NaN values. For this, at least sensor number and a 660 nm or 880 nm value is needed; i. e. the length of the array needs to be at least 2. A next function will search for all NaN values, and replace these with interpolations from surrounding values from the

same sample, sensor and wavelength.
Then the baseline drift of the raw data is removed. It is assumed that the first 45 seconds are in rest, and from this a slope coefficient is computed that is representative of the drift in that period. The drift is then removed by subtracting the computed slope times the frame number from the original, full array. While it is not certain that the baseline drift is an artifact, it makes the results of the two sensors easier to interpret.

After that the data is filtered with a lowpass, butterworth filter. The lowpassfilter has a cutoff frequency of 1.5 Hz. In this way high frequency noise in the time domain is reduced while conserving important information. This cutoff frequency is based on the measuring cycle that will be described as seen in figure 2.8, where there is less important information above 1.5 Hz. No highpassfilter is used, as that would delete all DC data.

2.5.2 StO_2 computation

After filtering, the absorbance for each color is determined and saved as a value. This is done as follows, as a function of incident light intensity and resultant light intensity[34, 35, 36].

$$A(\lambda) = ln\frac{I_0(\lambda)}{I(\lambda)} \tag{2.14}$$

Recognize the intensity I as defined in equation 1.2. The absorption value is representative of the amount of light that is absorbed by the tissue. The photodiodes are able to measure the photocurrent, denoted by N. Remember that $I \propto N$[30]. Remember also that after a pathlength of 1 mm, the light has scattered so much in the tissue that the initial direction has become irrelevant for the direction at that point [21]. This means that the detected photocurrent is not dependent on the angle to the Lambertian emitter, only on photodiode area. This is the same for the detected N_A, and the to be detected N. When including equation 2.11, this results in:

$$A(\lambda) = ln\frac{I_0(\lambda)}{I(\lambda)} = ln\frac{N_0(\lambda)}{N(\lambda)} = ln\frac{117 \cdot N_A(\lambda)}{N(\lambda)} \tag{2.15}$$

When equation 2.14 and 1.2 are combined, it is possible to compute the the concentration of a chromophore:

$$A(\lambda) = ln\frac{I_0(\lambda)}{I_0(\lambda)e^{-\mu(\lambda)\cdot d\cdot C\cdot DPF}} = \mu(\lambda)\cdot d\cdot C\cdot DPF$$

However, the absorbance of a certain wavelength is a function of the absortion by multiply chromophores. The absorbance as a result of solutions of multiple chromophores x and y is additive[34]. This means that:

$$A_{x+y}(\lambda) = A_x(\lambda) + A_y(\lambda) = \mu_x(\lambda)\cdot d\cdot C_x\cdot DPF + \mu_y(\lambda)\cdot d\cdot C_y\cdot DPF \tag{2.16}$$

As tissue is a strong scatterer of light, the distance is not representative of the actual path the light has taken as discussed in 1.5.4. It is however still necessary to take this into account to obtain realistic values of oxygen saturation. A typical DPF for various areas as the forearm and forehead range from 3.9-4.4 and 5.9-6.5 repectively[37]. For this report, an DPF is approximated of 5. The pathlength is defined as a half circle with a diameter equal to the distance from the LED to the photodiode, to approximate the path as seen in figure 1.9.
Then the concentration of each chromophore needs to be computed. The absorption is not dependent on one chromophore, but the combination of the concentrations of multiple chromophores. The extinction coefficients of oxy[heme] and deoxy[heme] at 660nm and 880nm used are as seen in figure 1.5. The sum of all heme is indicated with total[heme].
Substituting extinction coefficients, pathlengths and DPF for oxy[heme] and deoxy[heme] at 660nm and 880nm into equation 2.16 gives a system of two equations with two unknown concentrations:

$$\begin{cases} A_{total[heme]}(660nm) = & \mu_{deoxy[heme]}(660nm)dC_{deoxy[heme]}DPF \\ & +\mu_{oxy[heme]}(660nm)dC_{oxy[heme]}DPF \\ A_{total[heme]}(880nm) = & \mu_{deoxy[heme]}(880nm)dC_{deoxy[heme]}DPF \\ & +\mu_{oxy[heme]}(880nm)dC_{oxy[heme]}DPF \end{cases} \tag{2.17}$$

This system of equations is then solved to obtain the concentrations of deoxy[heme] and oxy[heme] for each frame in a sample[35]. Note that this assumes all absorption is caused by deoxy[heme] and oxy[heme], while other tissues are not taken into account. After, the oxygen saturation is determined by taking:

$$StO_2 = \frac{C_{oxy[heme]}}{C_{deoxy[heme]} + C_{oxy[heme]}} \cdot 100 \tag{2.18}$$

Because the StO_2 value that is measured is not absolute, all of the values are subtracted from the first measured value when plottinng. In this way it shows the relative difference to the first measurement and may it be possible to compare the change of oxygen saturation over time between sensor 0 and 1(note: not the differential!).
Lastly, there are several plotting options: for absorbance; concentration; and oxygen saturation. At least 1 sample, and at most 3 samples can be given to plot in the figure. As different steps in the process are saved as variables, evaluation of the steps is possible. In the script are several warning messages built in, to note physically not possible results.

2.5.3 Calibration

For calibration some of the same steps are taken as for the samples and some different steps. The format of the input is the same, and comes from the separate calibration measurements. The output is a single value that is representative of the mean of the file. First the data is loaded into the file and missing values are

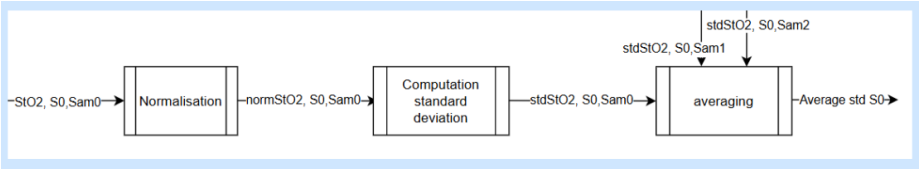

Figure 2.11: Flowchart of the computation of the normalized, average standard deviation per sensor of a set. The sensors in samples of a sets will be normalized and the standard deviation will be determined. From this an average is taken.

interpolated, using the same function as for the samples. Then the data is also filtered through the same lowpass filter to remove time-domain high frequency noise.
Then the outliers are removed. If a value in the file is bigger than a threshold times the amount of the median value of the file, set here as 4, then that value will be replaced by the median value. This removes any big spikes. Then the final computation is done, where the measured photocurrent N_A is determined by computing the mean value for every wavelength on every sensor.

2.6 Results acquisition

2.6.1 Calibration

For results, first the quality of the LEDs, detectors and calibration method will be evaluated. The slope of the data will be computed. In this way, it is seen how much drift there is present in the sensors and if this drift changes over different measurement dates. The goal is to evaluate the stability of the sensitivity of the photodiodes and the output of the LED during a measurement.
Also, the mean will be computed of the detected photocurrent. The goal is to evaluate the calibration method and stability of output of the LEDs by evaluating a change in mean between different measurements.

2.6.2 StO_2

As mentioned in section 2.5.2, different steps in the process are saved as variables. These variables are plotted and compared, to check for any surprising results. It is expected that all absorbances are positive and all concentrations are also positive. It is expected that the mean of the absolute oxygen concentration for each sample is positive and under 100%. To evaluate if the sensors can detect a change in oxygen saturation, the standard deviation between the sensors are compared. For this, first the oxygen saturation is determined. This is then normalized by dividing it by the mean of the absolute oxygen saturation. Then the standard deviation is calculated, after which the standard deviations are averaged with the values obtained by the same sensors from the same set. See also figure 2.11. The same steps are then taken for the other sensor in the

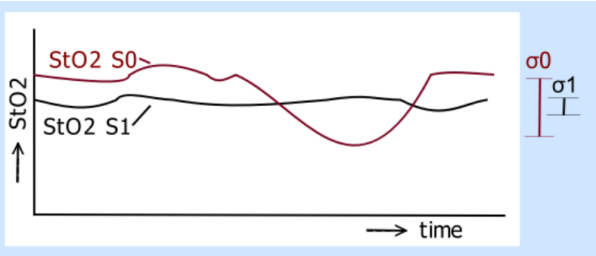

Figure 2.12: Graphic support imaging the effect of the cuff on the standard deviation. If there is a dip caused by the cuff, this could cause a higher standard deviation. The symbol σ stands for the standard deviation.

set, and the sensors in the second set. It is hypothesized that because the cuff temporarily lowers the oxygen saturation, sensor 0 will have a bigger deviation from the mean and thus a larger standard deviation than sensor 1 for both sets, see figure 2.12.

Chapter 3

Results

3.1 Calibration

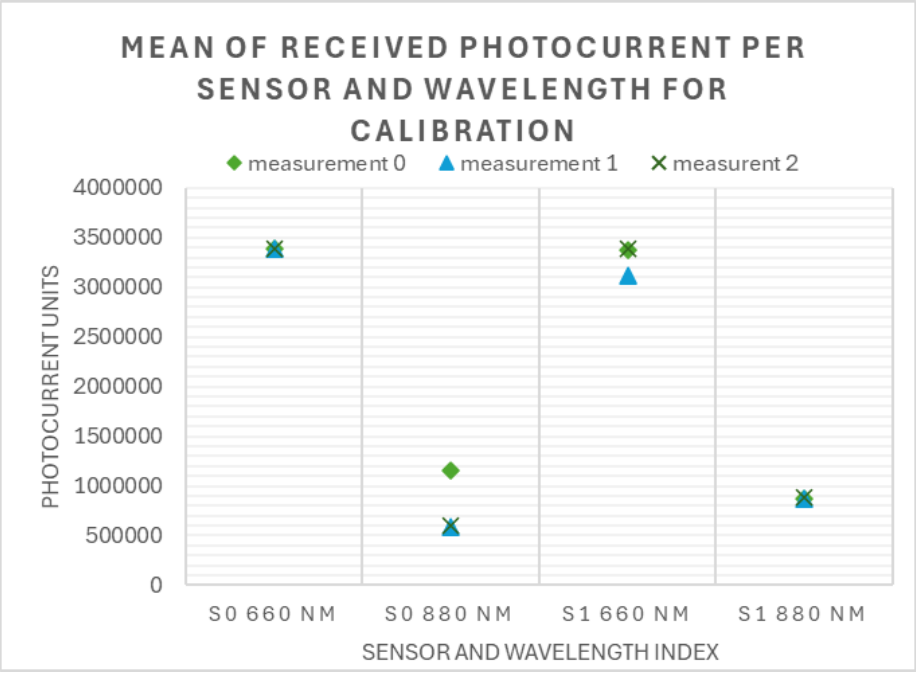

Figure 3.1: Comparison of the mean as detected by the photodiode during the calibration measurements.S0 is sensor 0 and S1 is sensor 1.

In figure 3.1 the mean is visible of the calibration value N_A. For sensor 0 at 660 nm the mean of the highest value is 1.0015 times as high as the lowest value. For sensor 0 at 880 nm the largest value was 1.954 times as high as the lowest

value. Do note that this is for the same sensor. It is also of note that the average photocurrent for red light is 4.04 times as high as the photocurrent of infrared light.

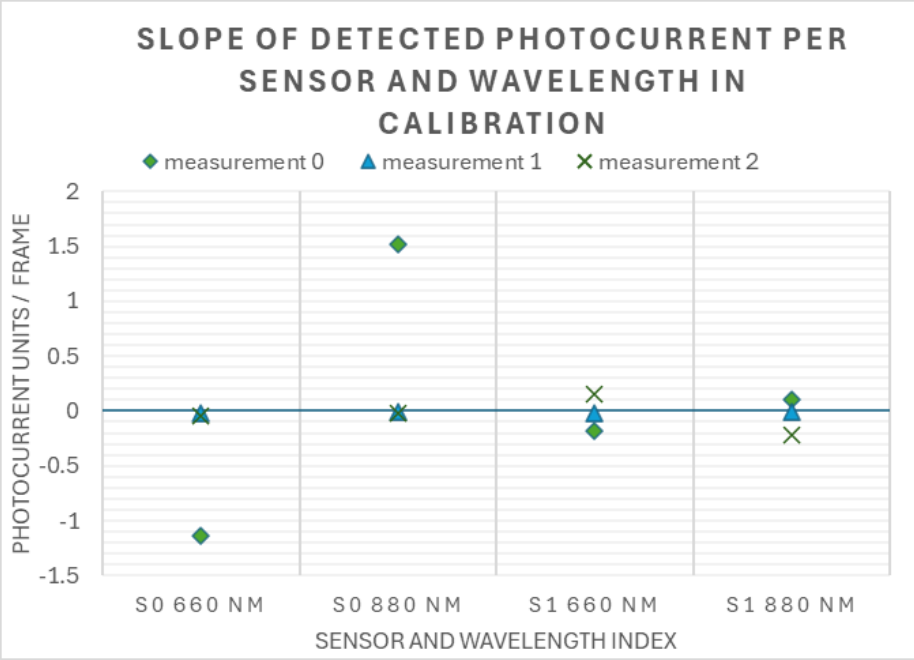

Figure 3.2: Comparison of the slope of the drift that is present in calibration measurements. S0 is sensor 0 and S1 is sensor 1.

In figure 3.2 the slope the detected N_A is visible. The biggest slope is for sensor 0, for 880 nm with 1.52 photocurrent units per frame. In a sample of 120 seconds, and thus $t \cdot framerate = 120 \cdot 25 = 3125$ photocurrent units. In combination with the mean as shown in figure 3.1, this would mean an increase of 0.41 % at the end of the measurement. It is visible that the drift of a sensor does not stay the same over time; for measurement 0 to measurement 1 the drift for the same sensor for the same wavelength changes.

3.2 Cuff measurements

3.2.1 Set 1

In figure 3.3 the StO2 is plotted. This is in deviation from its value at the start of the measurement, at t=0. The mean StO2 for S0 was 64.3%, 64.4% and 64.4%. The mean StO2 for S1 was 65.1%, 65.1% and 66.0% . This is for sample

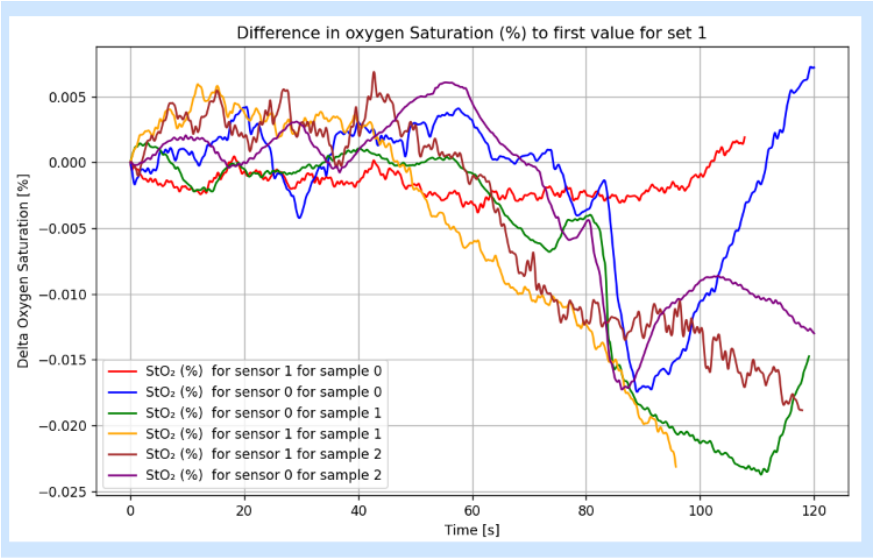

Figure 3.3: An image of the plotted oxygen saturation of set 1. The values are not absolute, but relative to the first value.

0, 1 and 2 respectively. Notice that for sensor 0 the mean StO2 was lower than sensor 1 for every sample.

	Sam. 0		Sam. 1		Sam. 2	
	S0	S1	S0	S1	S0	S1
Mean A(660nm)	6.50	6.50	6.50	6.51	6.49	7.10
Mean A(880nm)	5.05	5.14	5.05	5.15	5.04	5.74
Mean $C_{deoxy[heme]}[10^{-3}]$	1.83	2.30	1.83	1.82	1.82	1.97
Mean $C_{oxy[heme]}[10^{-3}]$	3.30	3.40	3.30	3.40	3.30	3.83

Table 3.1: The average values of some datasets as computed with the software, to give an indication of values in the datasets. $A(\lambda)$ shows the average absorbance at that wavelength.

In table 3.2.1 the mean values for different samples for concentration and absorbance are seen. All values in the table are positive. For set 2, not pictured, this was the same.

3.2.2 Set 2

In figure 3.4 the computed deviation of StO2 for set 2 is plotted. The mean of absolute oxygen concentration as measured for set 2 is 54.1%, 54.1% and 58.2% for sensor 0 and 65.1%, 65.1% and 65.1% for sensor 1, for sample 0, 1 and 2 respectively.

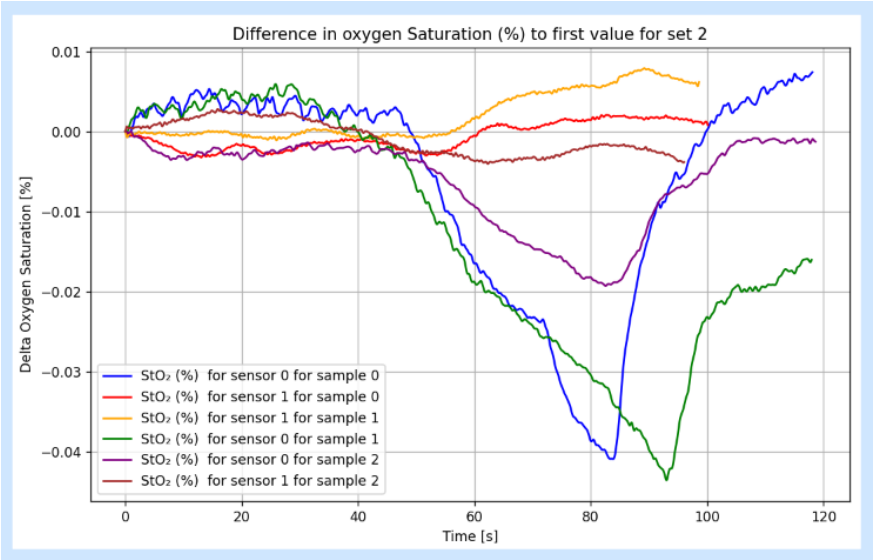

Figure 3.4: Deviation of oxygen saturation from its starting value, for set 2. The values are not absolute, but it show the difference to the first value

3.2.3 Average standard deviation

Table 3.2 shows the normalized standard deviation computed as in figure 2.11. It is seen that for both set 1 and 2 the standard deviation is higher for sensor 0 than sensor 1. The difference is bigger for set 2 than for set 1.

normalized standard deviation	S0	S1
set 1 $[10^{-5}]$	11.0	8.56
set 2 $[10^{-5}]$	20.8	3.45

Table 3.2: The average of the normalized standard deviation of the StO2 value for each set and sensor.

Chapter 4

Discussion

4.1 Measurement discussion

4.1.1 Other NIRS mode and pathlenght

There are more types of near infrared spectrometer methods. For this report there has been made use of continuous wave NIRS. This means incident light is used of a constant intensity. A disadvantage of this technique is that pathlength is unknown, which is one reason that the absolute concentrations cannot be known. There are however other types of NIRS that are used for which the absolute pathlength can be deduced. One of these techniques is time-domain spectroscopy. Instead of a continuous wavelength, a short pulse of light is send out. Then the light as detected by the photodector can be plotted over time, after which time of flight can be used to determine pathlength. The maximum sample rate of the MAX30102 is 3200 samples per seconds, which is equal to a sample time of 0.3125 ms. Its minimal pulse width is $69\mu s$. For time-domain spectroscopy, the detector needs to have resolution that is in sub-nanosecond, and a pulse width that is also sub picosecond. The sensors that are used in this report are thus not of sufficient temporal resolution to be able to use time-domain spectroscopy[7, 24, 38].

4.1.2 MAX30102 sensor

The MAX30102 contains internal ambient light rejection in the datatransfer from the photodiode to the ADC conversion. This has possibly influenced outcomes[38].

4.1.3 Validation

One of the validation problems was the small measurement set. Because of the small sample size, the some conclusions could not be certain. There was also no golden standard used; a pulse oximeter would give a different fraction of blood,

and blood gas analysis would be invasive. For validation, a commercial NIRS sensor could be used in future research.

4.2 Results discussion

4.2.1 Calibration; mean and shift

In figure 3.2 it is seen that for the same sensors any shift in mean for one wavelength does not necessarily correlate with a shift for the other wavelength in the same sensor. For sensor 0, there is a big accordance with itself for 660 nm and less accordance with itself for 880 nm. If the sensor itself would have shifted and the distance to the mirror would have grown, you would expect similar shift in both wavelengths. This can indicate inconsistencies in either the used sensor or the calibration method.

The path of light from LED to photodiode is very sensitive to movement and placement. This could affect the scale of change in oxygen saturation. Any tensing of the muscle was also very visible in the measurement, as it would give spikes in oxygen saturation. Testing had to be done in complete rest of the arm and fingers. When designing the device for patient use this needs to be taken into account, as it may be more difficult to control patient movement.

The LED brightness that was used was the default setup of the library. This set the red LED to a current that was higher than the infrared LED current[39]. Results could have been easier to compare if the current was equal, and this difference could have been the reason the mean red photocurrent is larger than the measured mean infrared photocurrent.

4.2.2 Drift

The drift removal is less accurate as time progresses. If either individual sensors or lasers were degrading faster than the other, you could see this in your results as a change in oxygen saturation if there was no drift removal. The drift does not have a constant derivative over time, as the slope is different between the measurements as seen in figure 3.2. This means that you cannot simply subtract it from the data. This could give problem in more dynamical systems, where you don't know whether a change in tissue oxygen saturation is caused by drift or signal.

4.2.3 $StO2$

As seen in the figure 2.9, it is expected that the oxygen saturation goes down and then up again. This is clearly visible in figure 3.4. It is however less visible in figure 3.3, what can indicate inconsistencies in the measurement cycle, method or computations in developed NIRS sensor.

The blood oxygen saturation of venous blood is around 70%, and arterial blood has blood oxygen saturation of around 95 %. The computed mean oxygen saturation between 54% and 66% is low, but not unreasonable when taking into account the non-absolute nature of the used NIRS method. It is also visible that the values of mean oxygen saturation are different from eachother, when placed in the same area. If the NIRS method is able to pick local, static differences in oxygen saturation the translation to breast cancer detection would be more apparent. For now this is not the case, so future research could look into ways to either be able to pick up this static local difference or to possibly use a induced change in tissue oxygen saturation.

4.2.4 Normalized standard deviation

The expectation was that the standard deviation of sensor 0 would be bigger than for sensor 1. When looking at table 3.2 this seems to indeed be the case for both sets, what would indicate that the NIRS sensor is able to pick up changes in oxygen saturation. However because the same sensors were used for every measurement, it is not possible to confirm the larger standard deviation is caused by the changing oxygen saturation or possible differing quality of the sensors. By changing up the sensors instead of using the same physical ones per measurement and getting more measurement sets, more could be said about this.

For the same table, the difference between sensor 0 and sensor 1 is bigger for set 2 than for set 1. This is in accordance with figure 3.1 and 3.2, where for set 2 the expected dip in the curve is easier to recognize than for set 1.

4.3 Future recommendations

4.3.1 Distance between sensors

An advantage of NIRS is that its able to measure at different depths. The depth to be measured is changed by making the distance between the sensor and light emitter larger of smaller [26]. The sensor that is used, the Gy-MAX30102 has a fixed distance between sensor and light emitter, so it was possible to only measure at only one depth. For future research, the possibility of measuring at different depths can be investigated.

4.3.2 Sensor qualifications

Other specifics of the sensor are not yet determined. These are measuring depth; spatial resolution; depth resolution; significance. It is also not proven whether the tumor will be able to be visualized, or which differences in blood oxygen can be indicative of a tumor. Research on the resolution needed to detect hypoxic region is not conclusive, however Dewhirst et al. found a spatial resolution of $1mm^2$ to be sufficient[40].

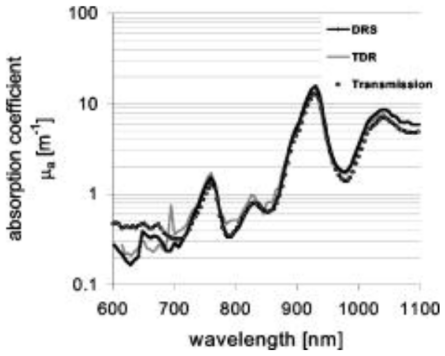

Figure 4.1: Absorption spectrum for mammalian fat in solid and liquid state. Multiple types of spectroscopy are used to determine these terms: distance resolved; time resolved; and transmittance spectroscopy [42].

Blood vessel that are larger than 1 mm usually contribute little to signal, as all is absorbed. This is useful to know when picking a measurement spot; it needs to be well vascularised, but with preferably smaller vessels[24].

For future research some approximations and assumptions can be worked out. Especially the differential pathlength factor or the pathlength of light.

4.3.3 Breast composition

OxyForce will eventually be meant for diagnostic purposes on the breast. Because temporarily cutting off circulation to the breast was more complicated, measurements were done on the arm. The composition of the underarm is quite different than the breast; breast contain a lot of fat and fibroglands. The breast density also varies between persons, what could have influence in the differential path length[41].

Fat also has absorption in the higher relevant wavelengths, see figure 4.1. This needs to be accounted for when developing the OxyForce. A way this could be accounted for is to incorporate a sensor and light source of a third wavelength, as then the system of equation as seen in equation 2.17 can be solved for another substance.

Chapter 5

Conclusion

The results are promising for showing that the NIRS sensor is able to pick up in vivo changes in the oxygen saturation. If the NIRS sensor could pick up static differences in oxygen saturation, the translation to breast cancer detection would be more apparent. This research is not conclusive on the ability to pick these up. However, some approximations were made which influence the repeatability of the results. For future research, working out these approximations and unknowns could give a better indication about the ability to pick up these static differences. It is also recommended to use LEDs with a stable output. If it is not possible to pick these up, it would be recommended to research ways to possibly use a changing oxygen saturation to non-invasively detect tumors.

DISCLAIMER

The code that is associated with this document is created with help of generative AI

Bibliography

[1] Hyuna Sung et al. "Global Cancer Statistics 2020: GLOBOCAN Estimates of Incidence and Mortality Worldwide for 36 Cancers in 185 Countries". en. In: *CA Cancer J Clin* 71.3 (Feb. 2021), pp. 209–249.

[2] G T Vondeling et al. "Burden of early, advanced and metastatic breast cancer in The Netherlands". en. In: *BMC Cancer* 18.1 (Mar. 2018), p. 262.

[3] Andrea R Marcadis, Luc G T Morris, and Jennifer L Marti. "Relative survival with early-stage breast cancer in screened and unscreened populations". en. In: *Mayo Clin. Proc.* 97.12 (Dec. 2022), pp. 2316–2323.

[4] Elaine N Marieb and Katja N Hoehn. *Human Anatomy & Physiology, Global Edition*. en. 10th ed. London, England: Pearson Education, June 2015.

[5] Ahmet Çağdaş Seçkin, Çetin Gençer, and Mustafa Yıldırım. "Deep Learning Structures used in Pulmonary Cancer Diagnosis". In: Feb. 2021. ISBN: 978-625-7342-78-0.

[6] Roland N Pittman. *Oxygen transport*. en. Morgan & Claypool Life Sciences, 2011.

[7] Thomas J Barstow. "Understanding near infrared spectroscopy and its application to skeletal muscle research". en. In: *J. Appl. Physiol.* 126.5 (May 2019), pp. 1360–1376.

[8] Scott Prahl. *Optical absorption of hemoglobin*. `https://omlc.org/spectra/hemoglobin/`. Accessed: 2024-11-20.

[9] Gonçalo Ávila et al. "Mal-positioning of a dialysis catheter: One lumen with arterial blood and the other with venous blood?" en. In: *J. Vasc. Access* 25.2 (Mar. 2024), pp. 681–684.

[10] Hannah Schobel. "Mixed Venous Oxygen Saturation". In: *Anesthesiology Core Review: Part Two Advanced Exam*. Ed. by Brian S. Freeman and Jeffrey S. Berger. New York, NY: McGraw-Hill Education, 2016. URL: `accessanesthesiology.mhmedical.com/content.aspx?aid=1135738187`.

[11] Larbi Boubchir et al. “EEG error potentials detection and classification using time-frequency features for robot reinforcement learning”. en. In: *Annu. Int. Conf. IEEE Eng. Med. Biol. Soc.* 2015 (Aug. 2015), pp. 1761–1764.

[12] T Dunn. “Oxygen and cancer”. en. In: *N. C. Med. J.* 58.2 (Mar. 1997), pp. 140–143.

[13] Nicole M Anderson and M Celeste Simon. “The tumor microenvironment”. en. In: *Curr. Biol.* 30.16 (Aug. 2020), R921–R925.

[14] Peter Vaupel et al. “Hypoxia in Breast Cancer”. In: *Oxygen Transport to Tissue XXVI*. Springer US, 2005, pp. 333–342.

[15] K Lundgren, C Holm, and G Landberg. “Hypoxia and breast cancer: prognostic and therapeutic implications”. en. In: *Cell. Mol. Life Sci.* 64.24 (Dec. 2007), pp. 3233–3247.

[16] S Nioka and B Chance. “NIR spectroscopic detection of breast cancer”. en. In: *Technol. Cancer Res. Treat.* 4.5 (Oct. 2005), pp. 497–512.

[17] Danny Castro et al. “Arterial blood gas”. en. In: *StatPearls*. Treasure Island (FL): StatPearls Publishing, Jan. 2024.

[18] Ryan C Perez et al. “Functional imaging of hypoxia: PET and MRI”. en. In: *Cancers (Basel)* 15.13 (June 2023).

[19] James P B O’Connor, Simon P Robinson, and John C Waterton. “Imaging tumour hypoxia with oxygen-enhanced MRI and BOLD MRI”. en. In: *Br. J. Radiol.* 92.1095 (Mar. 2019), p. 20180642.

[20] *Understanding Pulse Oximetry SpO2 Concepts*. Available at `https://www.documents.philips.com/doclib/enc/fetch/586262/586457/Understanding_Pulse_Oximetry.pdf`. Philips Medical Systems. Eindehoven, The Netherlands, Jan. 2003.

[21] Paul D Mannheimer. “The light-tissue interaction of pulse oximetry”. en. In: *Anesth. Analg.* 105.6 Suppl (Dec. 2007), S10–S17.

[22] Klaus D Torp et al. “Pulse oximetry”. en. In: *StatPearls*. Treasure Island (FL): StatPearls Publishing, Jan. 2024.

[23] Brant B Hafen and Sandeep Sharma. “Oxygen saturation”. en. In: *StatPearls*. Treasure Island (FL): StatPearls Publishing, Jan. 2024.

[24] Siana Jones et al. “Recent developments in near-infrared spectroscopy (NIRS) for the assessment of local skeletal muscle microvascular function and capacity to utilise oxygen”. en. In: *Artery Res.* 16.C (Dec. 2016), pp. 25–33.

[25] Amanda Cheung et al. “Detection of hypoxia by near-infrared spectroscopy and pulse oximetry: a comparative study”. In: *Journal of Biomedical Optics* 27 (July 2022). DOI: `10.1117/1.JBO.27.7.077001`.

[26] Yafeng Pan, Guillermo Borragán, and Philippe Peigneux. "Applications of Functional Near-Infrared Spectroscopy in Fatigue, Sleep Deprivation, and Social Cognition". In: *Brain Topography* 32 (Nov. 2019). DOI: 10.1007/s10548-019-00740-w.

[27] Ivan Moreno and Ching-Cherng Sun. "Modeling the radiation pattern of LEDs". In: *Opt. Express* 16.3 (Feb. 2008), pp. 1808–1819. ISSN: 1094-4087. DOI: 10.1364/OE.16.001808.

[28] Angelo Arecchi, Tahar Messadi, and R. John Koshel. *Lambertian and Isotropic Models*. Vol. FG11. SPIE, Aug. 2007. DOI: 10.1117/3.764682.p33.

[29] Jinjiang Wang, Wenyao Liu, and Huaiyu Cai. "Monte Carlo simulation of surface Lambertian source". In: *Third International Conference on Photonics and Imaging in Biology and Medicine*. Ed. by Qingming Luo et al. Wuhan, China: SPIE, Dec. 2003.

[30] Caroline Boudoux. *Fundamentals of biomedical optics*. en. Jan. 2017.

[31] Rick Bezemer et al. "Assessment of tissue oxygen saturation during a vascular occlusion test using near-infrared spectroscopy: the role of probe spacing and measurement site studied in healthy volunteers". en. In: *Crit. Care* 13 Suppl 5.Suppl 5 (Nov. 2009), S4.

[32] Stephen C. Kanick et al. "Continuous monitoring of interstitial tissue oxygen using subcutaneous oxygen microsensors: In vivo characterization in healthy volunteers". In: *Microvascular Research* 124 (2019), pp. 6–18. ISSN: 0026-2862. DOI: https://doi.org/10.1016/j.mvr.2019.02.002. URL: https://www.sciencedirect.com/science/article/pii/S0026286218301997.

[33] Andrew G Horn et al. "Post-occlusive reactive hyperemia and skeletal muscle capillary hemodynamics". en. In: *Microvasc. Res.* 140.104283 (Mar. 2022), p. 104283.

[34] *The Basics of UV-Vis Spectrophotometry: A Primer*. Available at https://www.agilent.com/cs/library/primers/public/primer-uv-vis-basics-5980-1397en-agilent.pdf. Agilent. July 2021.

[35] Joyce A. Wahr et al. "Near-Infrared spectroscopy: Theory and applications". In: *Journal of Cardiothoracic and Vascular Anesthesia* 10.3 (1996). Tee-Testing Competence Cardiac Complications in Noncardiac Surgery CPB and Adhesion Molecules Aortic Dissections, pp. 406–418. ISSN: 1053-0770. DOI: https://doi.org/10.1016/S1053-0770(96)80107-8. URL: https://www.sciencedirect.com/science/article/pii/S1053077096801078.

[36] Laura Porta. "Wearable NIRS sensor for oxygen level in human brain based on Arduino". In: (July 2023).

[37] B. Koirala et al. "Estimation of differential pathlength factor from NIRS measurement in skeletal muscle". In: *Respir. Physiol. Neurobiol.* 326 (Aug. 2024), p. 104283. ISSN: 1569-9048. DOI: 10.1016/j.resp.2024.104283.

[38] *MAX30102: High-Sensitivity Pulse Oximeter and Heart-Rate Sensor for Wearable Health*. Available at `https://www.analog.com/media/en/technical-documentation/data-sheets/MAX30102.pdf`. Maxim Integrated Products. 2018.

[39] devxplained. *MAX3010x-Sensor-Library*. [Online; accessed 3. Dec. 2024]. Dec. 2024. URL: `https://github.com/devxplained/MAX3010x-Sensor-Library/blob/main/src/MAX30102.cpp`.

[40] Mark W Dewhirst and Samuel R Birer. "Oxygen-enhanced MRI is a major advance in tumor hypoxia imaging". en. In: *Cancer Res.* 76.4 (Feb. 2016), pp. 769–772.

[41] Natalia Partain et al. "Mammographic density changes in surgical weight loss-an indication for personalized screening". en. In: *BMC Med. Imaging* 18.1 (Dec. 2018).

[42] R L P van Veen et al. "Determination of visible near-IR absorption coefficients of mammalian fat using time- and spatially resolved diffuse reflectance and transmission spectroscopy". en. In: *J. Biomed. Opt.* 10.5 (Sept. 2005), p. 054004.